Mühendislik Bilimleri ve Tasarım Dergisi
8(3), 931 – 942, 2020
e-ISSN: 1308-6693

Journal of Engineering Sciences and Design
DOI: 10.21923/jesd.784056

Araştırma Makalesi Research Article

A MICROLENS BY GALLIUM DOPED ZINC OXIDE-NANOANTENNA

Ekin ASLAN*, Erdem ASLAN

Department of Electrical and Electronics Engineering, Hatay Mustafa Kemal University, 31060 Hatay, Turkey

Keywords

Sierpinski Fractal, Microlens, Alternative Plasmonics, Plasmon Talbot Effect.

Abstract

Alternative plasmonics based fractal microlens are investigated. In this context, lensing performance of gallium-doped zinc oxide Sierpinski carpet-based fractal construction functionalized by conformal Talbot effect is analyzed for communication wavelength 1550 nm. Focusing via diffraction from these 2D finite-sized and two-iterated fractal lattice system is computationally demonstrated. In this regard, focusing performance parameters are computationally examined on the basis of geometrical parameter sweep and fractal generation via finite difference time-domain numerical simulations. Focusing efficiency > 50%, absolute efficiency > 18%, and focal depth larger than primary spot size are introduced by all computational samples. Moreover, a conformal Talbot effect is exhibited by this novel alternative plasmonics construction. A novel perspective based on alternative plasmonics by a newly adapted fractal design to optics is proposed. Thus, this fractal microlens is presented as a new planarized focusing platform, acting a conformal transformation optics device for light capturing tolerance and low-cost.

GALYUM KATKILI ÇİNKO OKSİT NANOANTEN İLE MİKROLENS

Anahtar Kelimeler

Sierpinski Fraktal, Mikrolens, Alternatif Plazmonikler, Plazmon Talbot Etkisi.

Öz

Alternatif plazmonik temelli fraktal metalensler araştırılmıştır. Bu bağlamda, 1550 nm iletişim dalga boyu için, konformal Talbot etkisi ile işlevselleştirilmiş galyum katkılı çinko oksit Sierpinski halısı tabanlı fraktal yapının mercekleme performansı analiz edilmiştir. Bu 2D sonlu boyutlu ve iki yinelemeli fraktal kafes sisteminden kırınım yoluyla odaklanma, nümerik olarak gösterilmiştir. Bu bakımdan odaklama performans parametreleri, geometrik parametre taramasına ve fraktal yinelemesine dayanarak zamanda sonlu farklar alanında simülasyonlar aracılığıyla incelenmiştir. Odaklanma verimliliği > 50%, mutlak verimlilik >% 18 ve birincil spot boyutundan daha büyük odak derinliği tüm nümerik numuneler tarafından sunulmuştur. Dahası, bu yeni alternatif plazmonik yapı tarafından konformal Talbot etkisi sergilenmektedir. Optiğe yeni uyarlanmış bir fraktal tasarım ile alternatif plazmoniklere dayanan yeni bir perspektif önerilmiştir. Böylelikle, bu fraktal mikrolens, ışık yakalama toleransı ve düşük maliyet için, konformal dönüşüm optik cihazı olarak hareket eden yeni bir düzlemselleştirilmiş odaklama platformu olarak sunulmuştur.

Alıntı / Cite

Aslan, E., Aslan, E., (2020). A Microlens by Gallium Doped Zinc Oxide-Nanoantenna, Journal of Engineering Sciences and Design, 8(3), 931-942.

Yazar Kimliği / Author ID (ORCID Number)

E. Aslan, 0000-0003-0933-7796
E. Aslan, 0000-0001-6829-9000

Makale Süreci / Article Process	
Başvuru Tarihi / Submission Date	22.08.2020
Kabul Tarihi / Accepted Date	17.09.2020
Yayım Tarihi / Published Date	24.09.2020

1. Introduction

In metasurface-based flat lenses, the intended optical mechanism can be ensured by spatial differences via aperiodically arranged and subwavelength-scatterers modeling optical wave fronts into required formworks (Minovich et al., 2015). Hence metalenses have presented functionalities for flat screens, integrated optics, mid-

* İlgili yazar / Corresponding author: ekin.aslan@mku.edu.tr

infrared photonics, and flat optical components simplifying fabrication, and improvements such as smaller-size, high performance, and better image quality (Li et al., 2019; Khorasaninejad et al., 2016; Byrnes et al., 2016; Lalanne and Chavel, 2017).

The design and fabrication of optical devices such as plasmonic biosensors (Aslan et al.,2019; Aslan et al.,2017; Aslan et al.,2017; Aslan et al.,2016; Aouani et al., 2013), plasmonic photodetectors (Berini, 2014), ultrafast modulators (MacDonald et al., 2009), and light sources (Liu et al., 2016) both in the infrared (IR) and in the visible spectral regions can find new facilities with the aid of plasmonic scatterers. Especially fractal plasmonics at multiple-scale-dimensions by their scale-invariant construction offer multispectral plasmonic behavior with self-similar resonances (Rosa et al., 2011; Yang et al., 2014; Gottheim et al., 2015). Resonators in fractal form, can also propound a new area for flat lens design. Fractal zone plates are latest lensing ones (Zang et al., 2019; Xia et al., 2019). Those diffractive plates in a characteristic fractal geometry with mm-scale dimensions can ensure lensing. Additionally, a study in literature has proposed a general fractal lattice growth model and significantly extended the scope of fractal application in optics for focusing light (Gao et al., 2018). Ergo, fractal plasmonic metalens designs can be a new class for light focusing.

In this study, a novel focusing concept using alternative plasmonic material instead of metals and fractal resonator geometry for 1550nm-communication wavelength is studied. Sierpinski carpet is a deterministic fractal described by Wacław Franciszek Sierpiński in 1916 (Mandelbrot, 1982). In literature, it has been numerically shown that a gold nanocarpet arranged as Sierpinski carpet-like geometry feature a controlled broadband response and superfocusing for visible wavelengths (Volpe et al., 2011). Here, a lattice antenna system based on this fractal is proposed as 2D finite-sized fractal scatterers. Gallium-doped zinc oxide (GZO) $ZnO:Ga_2O_3$ is chosen as an alternative plasmonic material for nanoantenna formation. For focusing capability, GZO fractal nanoantennas in two iterations are opted. These finite sized resonators are designed on SiN membrane to increase the transmission while structure is illuminated from backward. Finite-difference time-domain (FDTD) method is used for 3D electromagnetic simulations of the structure. We present the geometrical parameter sweeps in a in a systematic trend and an interpretation for thickness sweep. We calculate metalens performance parameters such as full-width half-maximum (FWHM), efficiency (focusing efficiency η_{foc} and absolute efficiency η_{abs}), depth of focus (DF*;* focal depth), numerical aperture (NA), and fill-factor (FF) of these sub-wavelength plasmonic fractals. This study on a finite-sized 2D GZO Sierpinski carpet-like fractal-lattice nanoantenna system ensures novel opportunities within the framework of fractal metalenses with alternative plasmonic materials, and besides, exhibits plasmonic Talbot effect (Talbot, 1839) to be yield at the end of the results section.

2. Modeling and Design

Finite-sized 2D GZO lattice nanoantennas in the first two iterations of Sierpinski carpet-like geometry are computationally proposed in this work for the metalens design capable of focusing consonant with the Talbot effect. 3D electromagnetic simulations are performed using FDTD Solutions package. Perfectly match layers are taken for all boundaries during the simulations. Mesh size on the structure is set to 10 nm due to available hardware facilities and uniform mesh setting are used within 3D simulation volume. 100 nm-thick SiN suspended membrane is used to increase transmission under back-illumination by plane wave at 1550 nm-fiber communication wavelength. Schematic of the design is shown in Fig. 1. 1st and 2nd iterations of the Sierpinski carpet-like fractal nanoantenna geometry can be seen from the figure. The geometrical parameters of these iterations are the width of lattice elements W, the length of each lattice cell or element length L, the thickness of nanoantenna t_{GZO}, and the thickness of membrane t_{memb}. The gap distance of lattice is configured as $L - W$. In addition to these, a geometrical parameter analysis has been established as 8 different value-set for two iterations and all computational samples are denoted as Sample#i.A, where i and A (A = 1,2,...8) being iteration number and sample number in the same sector, respectively.

Dielectric function data of GZO from the ellipsometry data of a deposited GZO thin film from the literature are adapted to a Drude-Lorentz oscillator model $\varepsilon(\omega) = \varepsilon_\infty - \frac{\omega_p^2}{\omega^2 + i\omega\Gamma_p} + \frac{f_1\omega_1^2}{\omega_1^2 - \omega^2 - i\omega\Gamma_1}$ (Kim et al., 2013). Here, while the second term stands for Drude model, the third one represents Lorentz oscillator. The symbols in this equation express the background permittivity ε_∞, the unscreened plasma frequency ω_p, the carrier relaxation rate Γ_p, and the strength, the center frequency, and the damping of the Lorentz oscillator f_1, ω_1, and Γ_1 respectively (Naik et al., 2013). Thus, the optical properties of GZO are taken as ε_∞ = 2.475, ω_p = 1.927 eV, Γ_p = 0.117 eV, f_1 = 0.866, ω_1 = 4.850 eV, and Γ_1 = 0.029 eV (Kim et al., 2013). In order to determine lensing capability combined with Talbot effect, surface plasmon wavelength of GZO in air at 1550 nm-operating wavelength is calculated via surface plasmon wavelength λ_{SP} equation given by $\lambda_{SP} = \lambda_0 / Re\{\sqrt{\frac{\varepsilon_m \varepsilon_d}{\varepsilon_m + \varepsilon_d}}\}$, where ε_m and ε_d being dielectric function of the metal forming the structure and the environmental dielectric function of its environment, respectively (Barnes,

2006; Dennis et al., 2007). At λ_0 = 1550 nm, ε_d = 1 for air and $\varepsilon_m = \varepsilon_m' + i\varepsilon_m'' = -2.2433 + i1.0251$ from the fitted GZO data are used and λ_{SP} at λ_0 is calculated as 1264 nm. Refractive index of SiN is taken as 1.876 at 1550 nm (Vogt, 2015), which is used for suspended membrane. The corresponding structures are illuminated in the opposite z-direction under the x-polarization. Geometrical sweeps are supplied by taking L and W as multiples of $\lambda_{SP}/4$ and maximum z-value of GZO-layer is the thickness t_{GZO} in all simulations.

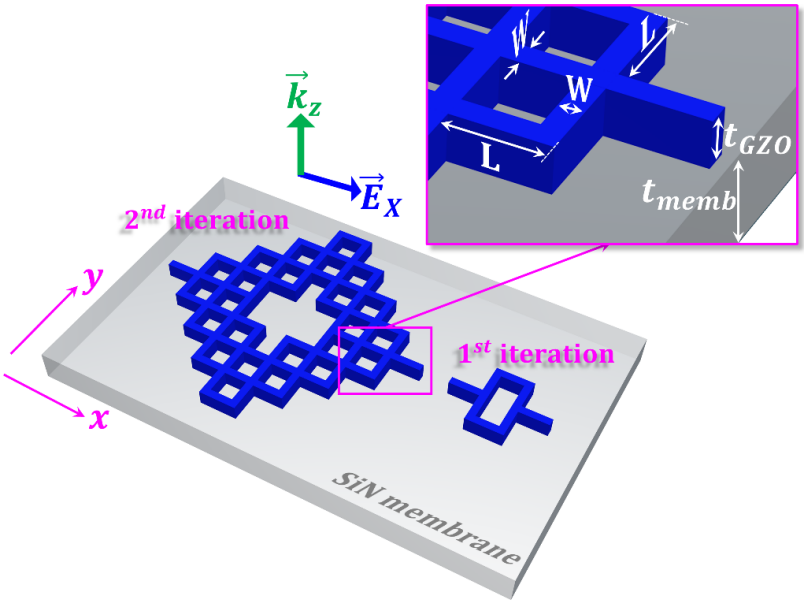

Figure 1. Schematic view of GZO-based Sierpinski Carpet nanoantenna designs at 1st and 2nd iterations.

3. Result and Discussion

In order to view geometrical parameter effects, a set of L and W analyses for each iteration is performed in a systematically manner. Additionally, an interpretation of t_{GZO} sweep for a specific iteration is given. Focusing performance of GZO-based Sierpinski carpet-like lattice at 1st and 2nd iterations is examined. The area with the normalized E-field intensity to the source intensity $|E|^2/|E_{in}|^2$ concentration and the center of this area are evaluated as focal spot and focal point, respectively. Since there will be multiple central focus, farthest focus point is indexed to be the priority and a focal length is expressed as f_k (k = 1,2,3,4...). f_1 always represents the primary or the first order focal length. The focal lengths are calculated as $f_k = z_k - t_{GZO}$, where z_k being the corresponding focal point. First of all, the effect of t_{GZO} variation on focal length-intensity balance of 1st iterated nanostructure with $L = \lambda_{SP}/2$ and $W = \lambda_{SP}/4$ is examined as shown in Fig. 2. As seen from this figure, primary focal spot attenuates while increasing t_{GZO}. According to the data taken from the monitor M_z, at the focal points z_1= 3061 nm, 3113 nm, 3153 nm, and 4037 nm for t_{GZO} = 100 nm, 150 nm, 200 nm, and 300 nm, respectively normalized intensities are 2.98, 2.33, 2.07, and 1.73. Here, the monitor arrangement given in Fig. 3a is exploited. For both iterations, the optimum thickness value is defined as t_{GZO} = 50 nm and results here are mostly presented for t_{GZO} = 50 nm over the primary focal point.

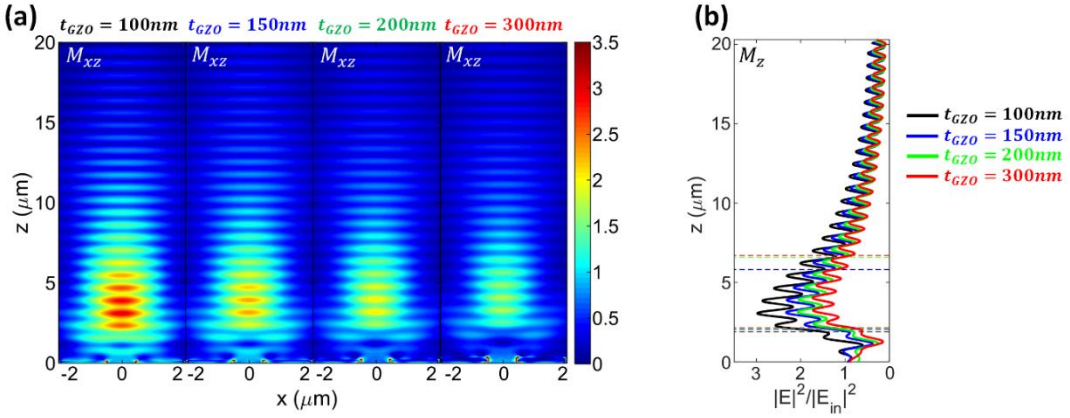

Figure 2. (a) Normalized intensity distribution maps on vertical monitor M_{xz} for the numerical sample with $L = \lambda_{SP}/2$ and $W = \lambda_{SP}/4$, each inner block from left to right stands for a different t_{GZO} value. **(b)** Normalized intensity curves of this sample on M_z for different t_{GZO}.

Starting from 1st iteration design, a systematic geometrical parameter-sweep is achieved. Accordingly, theoretical performance parameters of the fractal nanoantenna system at the desired optical frequency are assigned: FWHM spot size, the efficiency η, DF, NA, and FF (Yu and Capasso, 2014; Zhang et al., 2016; Gao et al., 2010; Tanriover and Demir, 2019; Aieta et al., 2012; Arbabi et al., 2015). FWHM spot size, the distance between two locations at which two intensity values are half of the maximum intensity value on related axes, is taken into account as focal spots during these calculations. Along-*x*-line and along-*y*-line monitors, M_x and M_y, respectively (Figs. 3a and 4a) are utilized to assign FWHM spot size of primary focal spots. Second performance parameter, efficiency is defined by two ways in the literature: the focusing efficiency η_{foc} is the ratio of the total light intensity at the focal spot to the total transmitted light and the absolute efficiency η_{abs} is the ratio of the total light intensity at the focal spot to the incident light intensity (Tanriover and Demir, 2019; Aieta et al., 2012; Arbabi et al., 2015). Here, η_{foc} and η_{abs} are calculated by using focal plane monitor M_{xy} (Figs. 3a and 4a). The other parameter, DF is the area tolerance in front of the lens in an acceptable focusing and taken as full-width half-maximum value (Gao et al., 2010) of the data from M_z (3(a) and 4(a)) along *z*-axis, $FWHM_z$. Additionally, NA which is a number that states the ability of a lens to resolve fine details in an observed object and derived from the mathematical formula $NA = n \sin\theta$. Here, n is the refractive index of the medium between the lens and the focal plane and θ is the angular aperture of the lens. After all, FF is also a significant parameter for microlenses in specially imaging applications. It is the fraction of microlens's active refracting area directing light to a destination to total contiguous area occupied by the microlens (Aieta et al., 2012). The active area (AA) and occupied area (OA) for this finite-sized design are the total area of the nanorings and the area with the largest nanoring's bigger diameters, respectively.

The first stage of iterative presentation is i = 1 for the proposed fractal structure. Finite-sized 2D metalens based on 1st iterated-GZO nanolattice with 50 nm-thickness is first examined at 1550 nm-operating wavelength, as in Fig. 3. Fig. 3a illustrates the schematic view of all used field monitors: *xz*-vertical, *yz*-vertical, *xy*-horizontal, along-*x*-line, along-*y*-line, and along-*z*-line monitors; M_{xz}, M_{yz}, M_{xy}, M_x, M_y, and M_z, respectively. Table 1 yields the analyzed performance parameter set for the computational samples Sample#1.A. The geometrical parameters L and W are variables here. While diffraction pattern of 1st iterated samples can be clearly observed through the *xz*-vertical and *yz*-vertical monitors (Fig. 3b,c,e,f), primary focal spot size can be seen through the *xy*-horizontal on the focal plane (Fig. 3h). Furthermore, along-*z*-line monitor M_z illustrates normalized *E*-field intensity values in the center of the system along illumination direction and DF (Fig. 3d,g). These graphs provide the determination of focal point, focal *E*-field intensity, FWHM spot size and DF values in Table 1. In order to define FWHM values along *x*- and *y*-axes, $FWHM_x$ and $FWHM_y$, respectively can also be seen from Fig. 3i where each block stands for a sample for 1st generation nanoantenna. Elliptical spot in Fig. 2f that can be represented by a circular area are used during determination of spot areas. Hence FWHM spot size is calculated by the geometric means of $FWHM_x$ and $FWHM_y$ (Li et al., 2017). $FWHM_x$ and $FWHM_y$ values for i = 1 are given in Table 2. Computational efficiencies obtained as a result of parameter changes in Table 1 are η_{foc} > 50% and η_{abs} > 20%. AA and OA parameters of the design with i = 1 used for calculation of FF in Table 1 are also given Table 2. From top to bottom for the samples with different L and fixed W, mostly increasing focal length and decreasing NA can be observed. On the other hand, for the samples with fixed L and different W, it is noteworthy that the efficiencies decrease. These all can be attributed to total structure width versus focal length as well as diffraction of far-fields, coupling of SPPs, and interference of near-fields (Li et al., 2011). Additionally, non-primary focal points z_k (k = 2,3) and their normalized intensities for i = 1 are given in Table 3.

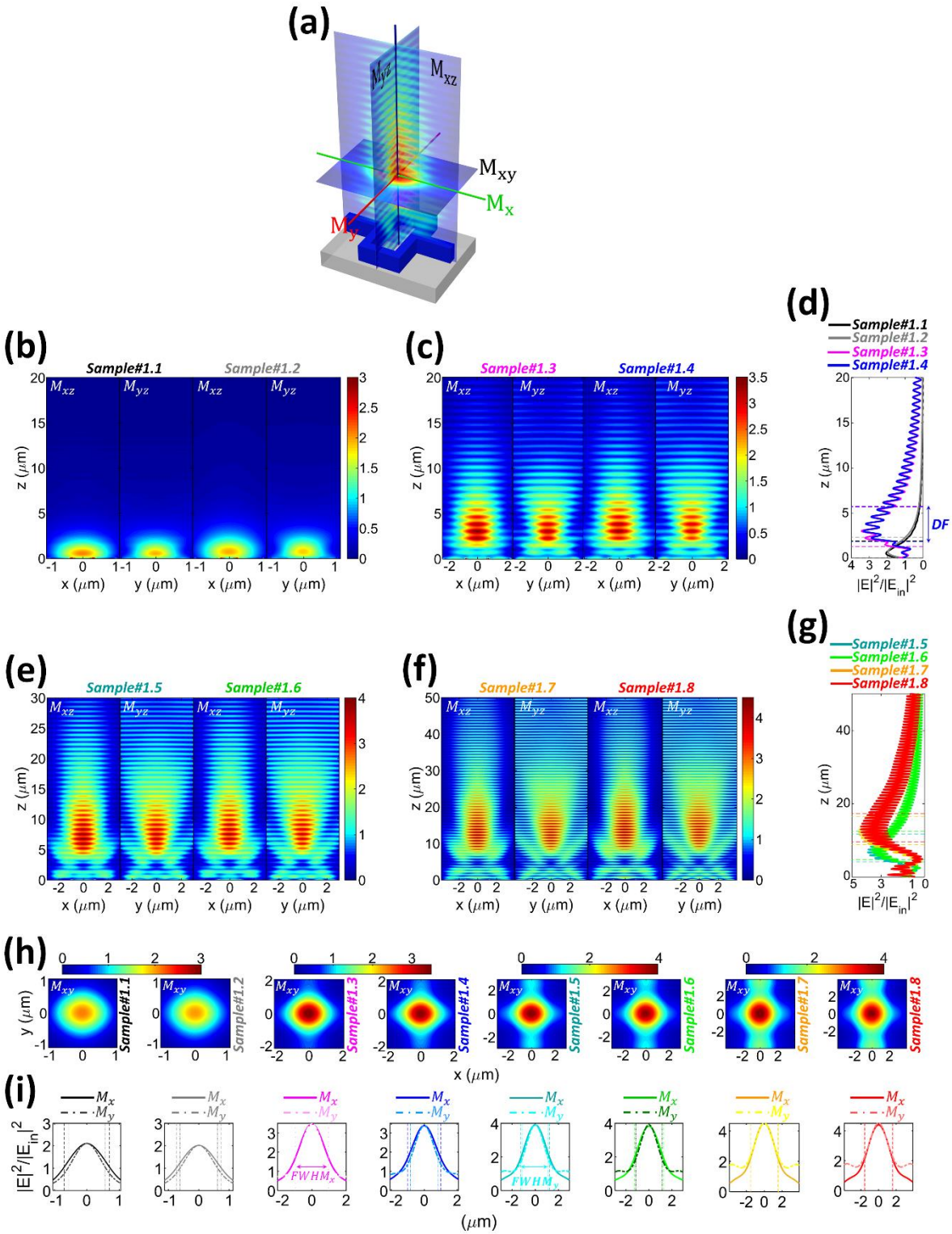

Figure 3. (a) The schematic view of monitor placement for 1st iteration-fractal nanoantenna (t_{GZO} = 50 nm). **(b,c,e,f)** Normalized intensity distribution maps on vertical monitors M_{xz} and M_{yz} each left-inner block-pair and each right-inner block-pair within a panel stand for a specific sample. **(d,g)** Normalized intensity curves on M_z **(h)** Focal intensity distributions on horizontal monitor M_{xy} and **(i)** normalized intensity curves on M_x and M_y.

Table 1. Geometrical parameter-sweep-table for 1st iteration nanoantenna with t_{GZO} = 50 nm. The first order focal lengths f_1, their maximum normalized intensity, FWHM, η_{foc}, η_{abs}, NA, FF and DF.

***1st iteration*, t_{GZO} = 50 nm**										
	L	W	f_1 (nm)	$\lvert E\rvert^2/\lvert E_{in}\rvert^2$	FWHM spot size (λ_0)	η_{foc} (%)	η_{abs} (%)	NA	FF	DF (λ_0)
Sample-	$\lambda_{SP}/2$	$\lambda_{SP}/8$	483	2.065	0.81	56.32	32.78	0.9	0.60	1.1984
Sample-	$\lambda_{SP}/2$	$\lambda_{SP}/4$	650	1.957	0.87	54.80	32.04	0.9	0.84	1.4695
Sample-	λ_{SP}	$\lambda_{SP}/8$	2950	3.432	1.23	55.96	28.82	0.8	0.47	2.8252
Sample-	λ_{SP}	$\lambda_{SP}/4$	2963	3.33	1.19	55.35	24.58	0.8	0.71	2.5172
Sample-	$3\lambda_{SP}/2$	$\lambda_{SP}/8$	6663	3.909	1.51	60.09	23.53	0.6	0.38	4.9608
Sample-	$3\lambda_{SP}/2$	$\lambda_{SP}/4$	7650	3.663	1.55	58.92	23.15	0.6	0.60	5.0351
Sample-	$2\lambda_{SP}$	$\lambda_{SP}/8$	12150	4.516	2.01	60.31	23.97	0.5	0.28	4.9866
Sample-	$2\lambda_{SP}$	$\lambda_{SP}/4$	12950	4.393	2.06	59.30	23.59	0.5	0.47	4.9899

Table 2. $FWMH_x$, $FWMH_y$, OA, and AA list for the geometrical parameter-sweep-table of 1st iteration nanoantenna with t_{GZO} = 50 nm at primary focal spot.

	$FWMH_x$ (nm)	**$FWMH_y$ (nm)**	**OA (nm²)**	**AA (nm²)**
Sample-1.1	1400	1119	1323092	798848
Sample-1.2	1478	1232	1897264	1597696
Sample-1.3	1904	1902	2571292	1198272
Sample-1.4	2008	1680	3395104	2396544
Sample-1.5	2483	2210	4218916	1597696
Sample-1.6	2552	2259	5292368	3195392
Sample-1.7	3030	3189	8712436	2396544
Sample-1.8	3104	3282	10285168	4793088

Table 3. Geometrical parameter-sweep-table of 1st iteration with t_{GZO} = 50 nm for non-primary focal points z_k (k = 2,3) and their normalized intensities.

	z_2 (nm)	$\frac{\lvert E\rvert^2}{\lvert E_{in}\rvert^2}$	z_3 (nm)	$\frac{\lvert E\rvert^2}{\lvert E_{in}\rvert^2}$
Sample-1.1	-	-	-	-
Sample-1.2	-	-	-	-
Sample-1.3	-	-	-	-
Sample-1.4	-	-	-	-
Sample-1.5	1257	1.387		
Sample-1.6	1287	1.508	-	-
Sample-1.7	2175	2.172	592	2.093
Sample-1.8	2185	2.286	598	2.511

As the next stage in systematic representation, theoretical performance parameters of 2nd iterated structure are determined as in Table 4. Herein, monitor arrangement in Fig. 4a is used for the calculation of these parameters. M_{xz} and M_{yz} (Fig. 4b,c,e,f) indicates that primary focal spots become distant due to bigger nanoantenna dimension together with bigger spot size and DF. While increasing W within the sample pairs with same L, focal intensities get lower (Table 4). It is also expected FF to get smaller due to OA and AA values of this 2nd iterated nanoantenna. FWHM spot size defined via $FWHM_x$ and $FWHM_y$ from M_{xy} (Fig. 4h), M_x, and M_y (Fig. 4i) take value as larger multiple of λ_0. Bigger spot size, smaller NA, and higher efficiencies are expected versus increasing lattice behavior (Arbabi et al., 2015). This can be associated with diffraction of far-fields, coupling of SPPs, and interference of near-fields (Li et al., 2011). But Talbot effect mechanism is also especially affected on efficiencies due to L value. This situation is explained below. Even so, Sample#2.A (A = 1,2,…8) exhibits η_{foc} > 50% and η_{abs} > 18% for the parameter-sweep set in Table 4. In addition, auxiliary parameters and non-primary focal points for 2nd iterated nanoantenna are given in Table 5 and Table 6, respectively.

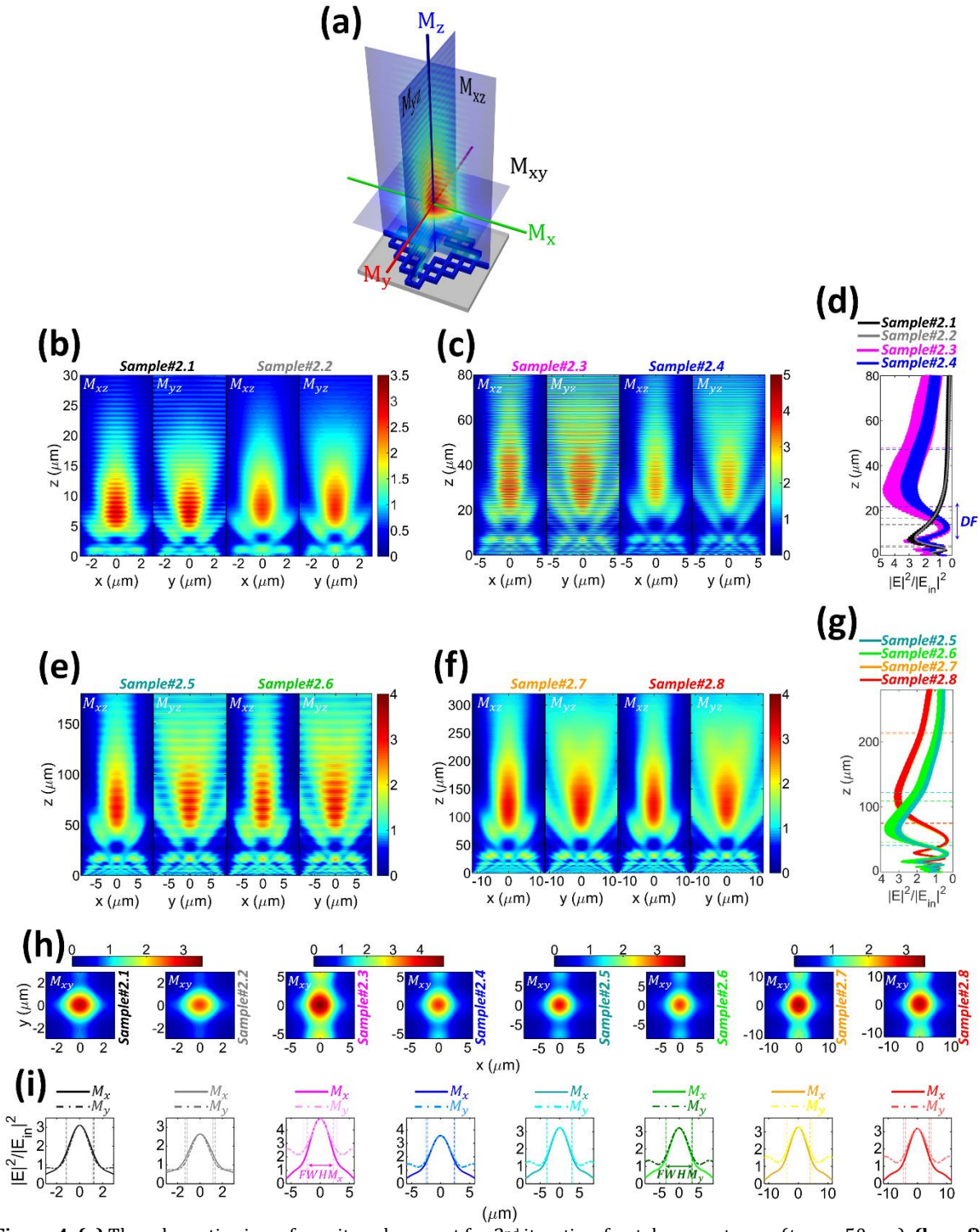

Figure 4. (a) The schematic view of monitor placement for 2nd iteration-fractal nanoantenna (t_{GZO} = 50 nm). **(b,c,e,f)** Normalized intensity distribution maps on vertical monitors M_{xz} and M_{yz} each left-inner block-pair and each right-inner block-pair within a panel stand for a specific sample. **(d,g)** Normalized intensity curves on M_z **(h)** Focal intensity distributions on horizontal monitor M_{xy} and **(i)** normalized intensity curves on M_x and M_y.

Table 4. Geometrical parameter-sweep-table for 2nd iteration nanoantenna with t_{GZO} = 50 nm. The first order focal points f_1, their maximum normalized intensity, FWHM, η_{foc}, η_{abs}, NA, FF and DF.

2nd iteration, t_{GZO} = 50 nm										
	L	W	f_1 (nm)	$\|E\|^2/\|E_{in}\|^2$	FWHM spot size (λ_0)	η_{foc} (%)	η_{abs} (%)	NA	FF	DF (λ_0)
Sample-	$\lambda_{SP}/2$	$\lambda_{SP}/8$	7212	3.11	1.52	52.43	20.80	0.9	0.45	6.3480
Sample-	$\lambda_{SP}/2$	$\lambda_{SP}/4$	7682	2.595	1.61	51.32	20.02	0.9	0.74	7.8976
Sample-	λ_{SP}	$\lambda_{SP}/8$	29030	4.833	3.28	64.66	27.25	0.6	0.25	16.810
Sample-	λ_{SP}	$\lambda_{SP}/4$	31186	3.578	3.08	54.57	21.36	0.6	0.45	16.454
Sample-	$3\lambda_{SP}/2$	$\lambda_{SP}/8$	64580	3.198	4.12	55.06	19.09	0.3	0.18	52.329
Sample-	$3\lambda_{SP}/2$	$\lambda_{SP}/4$	66310	3.795	4.23	56.87	19.70	0.3	0.33	40.889
Sample-	$2\lambda_{SP}$	$\lambda_{SP}/8$	11326	3.272	5.50	55.38	19.04	0.2	0.13	88.675
Sample-	$2\lambda_{SP}$	$\lambda_{SP}/4$	11634	3.251	5.60	54.63	18.99	0.1	0.25	89.625

Table 5. $FWMH_x$, $FWMH_y$, OA, and AA list for the geometrical parameter-sweep-table of 2nd iteration nanoantenna with t_{GZO} = 50 nm at primary focal spot.

	$FWMH_x$ (nm)	**$FWMH_y$ (nm)**	**OA (nm²)**	**AA (nm²)**
Sample-2.1	2474	2255	14504084	6590496
Sample-2.2	2686	2330	16276528	11982720
Sample-2.3	4421	5843	54546340	13780128
Sample-2.4	4589	4950	58016336	26361984
Sample-2.5	6163	6605	12015173	20969760
Sample-2.6	6331	6784	12531928	40741248
Sample-2.7	7825	9276	21132026	28159392
Sample-2.8	7906	9543	21818536	55120512

Table 6. Geometrical parameter-sweep-table of 2nd iteration with t_{GZO} = 50 nm for non-primary focal points z_k (k = 2,3,4,5) and their normalized intensities.

	z_2 (nm)	$\frac{\|E\|^2}{\|E_{in}\|^2}$	z_3 (nm)	$\frac{\|E\|^2}{\|E_{in}\|^2}$	z_4 (nm)	$\frac{\|E\|^2}{\|E_{in}\|^2}$	z_5 (nm)	$\frac{\|E\|^2}{\|E_{in}\|^2}$
Sample-2.1	1052	1.435	-	-	-	-	-	-
Sample-2.2	992	1.503	-	-	-	-	-	-
Sample-2.3	6698	3.37	2820	2.702	-	-	-	-
Sample-2.4	6526	2.576	2656	2.054	-	-	-	-
Sample-2.5	16000	2.057	8264	1.454	4386	1.225	-	-
Sample-2.6	16204	2.884	7716	2.07	4610	1.808	-	-
Sample-2.7	29220	2.105	15335	1.667	9920	1.413	6082	1.419
Sample-2.8	29226	2.203	15344	1.692	9932	1.611	6090	1.52

Computational and experimental microlens studies (Khorasaninejad et al., 2016; Aieta et al., 2012; Arbabi et al., 2016) are available in the literature for λ_0 = 1550 nm operation wavelength. By taking account of them, the work (Khorasaninejad et al., 2016) based on aperiodic arrangement of coupled α-Si rectangular resonators on a fused silica substrate proposes η_{abs} of 10% with FWHM spot size of $18.7\lambda_0$ and NA of 0.04. In that work, η_{abs} has been defined as the amount of power in the beam waist at the focal line, divided by the input power. The other one (Arbabi et al., 2016) composed of silicon nano-posts on glass has presented experimental results as η_{foc} of 65% with FWHM spot size of $1.77\lambda_0$ and NA of 0.46 while the one (Aieta et al., 2012) based on V-shaped gold nano-resonators on a silicon substrate has reported η_{foc} of 1% with FWHM spot size of $33\lambda_0$ and NA of 0.05. Present microlens studies based on plasmonic Talbot effect in the literature are employed for different operating wavelengths. One of them (Li et al., 2011) has presented a nanolens for 248 nm operating wavelength, composed of silver nanorings as the theoretical three-dimensional (3D) plasmon Talbot-effect study and examined a plasmon Talbot effect spanning from the near field to the far field. Then, Gao et al. (2010) have experimentally considered three patches of circular nanoholes on gold film for λ_0 = 500, 545, 670, and 780 nm. Moreover, Wang et al (2013) have computationally investigated the Ag, Au-, and Al-based nanolenses for various immersion media

such as air, SiO_2, Al_2O_3, and H_2O at wavelengths of 248, 365, and 442 nm. But they did not observe the Talbot effect and associated it with finite-size of the nanohole arrays. In our study, a fractal metalens system with first two iterations and alternative plasmonic material is investigated at 1550 nm-communication wavelength for the first time. A microlens with a larger NA can visualize finer however it ensures less efficiency and shallow depth of field. η_{foc} > 50% and η_{abs} > 18% are introduced by the computational samples in this study which represent a new alternative plasmonic approach to fractal lensing device with 50 nm-thick-GZO nanolattice resonators. Additionally, DF > FWHM is obtained for all computational samples and an appropriate geometrical parameter set can be consulted for desired focal behavior.

Table 7. Simulated integral Talbot positions τ_m, fractional Talbot positions τ'_m, and calculated Talbot distances τ_{cal} for Sample#2.3, Sample#2.4, Sample#2.5, Sample#2.6, Sample#2.7, and Sample#2.8.

2^{nd} ***iteration,***	τ'_1	τ_1	τ'_2	τ_2	τ'_3	τ_3	τ_{cal} **(non-paraxial)**	τ_{cal} **(paraxial)**
Sample-2.3	518	1271	-	-	-	-	1264 nm	2528 nm
Sample-2.4	398	1086	-	-	-	-	1264 nm	2528 nm
Sample-2.5	574	1344	2120	2876 nm	-	-	4964 nm	5688 nm
Sample-2.6	760	1532	2312	3062 nm	-	-	4964 nm	5688 nm
Sample-2.7	664	1466	2180	3028 nm	3746	4512	9434 nm	10112 nm
Sample-2.8	680	1486	2166	3116 nm	3755	4508	9434 nm	10112 nm

Talbot effect discovered in 1836 (Talbot, 1836) and explained by Rayleigh (1881) one of the focusing contraption in metalens constructions. This situation can be predicated on far-field diffraction, SPP coupling, and near-field interference (Li et al., 2011). As mentioned above, the prominence of the Talbot effect can also relatively reduce the efficiency of the primary focus for Sample#2.3, Sample#2.4, Sample#2.5, Sample#2.6, Sample#2.7, and Sample#2.8. According to Talbot phenomenon, scattering optical fields can exactly copy the pattern of a periodic structure at multiple distances, under illumination by a monochromatic plane wave (Talbot, 1836; Dennis et al., 2017; Li et al., 2017; Rayleigh, 1881; Mehdi et al., 2018a; Mehdi et al., 2018b; Wen et al., 2013). In ordinary Talbot effect, Talbot revivals are generated at the distance named as Talbot distance τ for each copied device pattern (Talbot, 1836; Dennis et al., 2007; Li et al., 2017; Rayleigh, 1881; Mehdi et al., 2018a; Mehdi et al., 2018b; Wen et al., 2013). The theoretical Talbot distance can be defined as $\tau = \frac{\lambda_e}{1-\sqrt{1-(\lambda_e/p)^2}}$ in the literature (Li et al., 2019) when array period of the structure is between λ_e and $2\lambda_e$. Here, λ_e is the effective operating wavelength calculated by λ/n for a periodic array with being n the refractive index of the medium and p the array period. τ becomes equal to $2p^2/\lambda_e$ with paraxial approach. Periodic metallic nanostructural arrays exhibit a complex coupling behavior between localized surface plasmon resonance (LSPR), Bloch wave surface plasmon polaritons (BW-SPPs) and Wood anomalies especially at optical frequencies due to their arrangements (Yu et al., 2013). Thus, a focusing fact related with a plasmonic Talbot effect observed under paraxial (Mehdi et al., 2018a) or non-paraxial (Mehdi et al., 2018b) conditions. Accordingly, non-paraxial and paraxial formulas between surface plasmon wavelength λ_{SP} and Talbot distance can be given as $\tau = \frac{\lambda_{SP}}{1-\sqrt{1-(\lambda_{SP}/p)^2}}$ and $2p^2/\lambda_{SP}$, respectively. However, some works showed lateral periodicity not to be necessary for Talbot revivals, and finite-sized 2D devices could exhibit Talbot self-imaging (Gao et al., 2010; Li et al., 2011; Wang et al., 2013; Yu et al., 2013). There can be some differences in light patterns of the devices under non-paraxial Talbot conditions beyond the paraxial limit. Herefrom, exact self-images with positions smaller than paraxial Talbot distances (Hua et al., 2012) can exist under the condition $1 \leq p/\lambda_{SP} < 2$. Hereof, a periodic grove-study on an Au film illustrates a non-paraxial plasmonic Talbot effect (Zhang et al., 2009). Here $p = L$ and the condition $1 \leq p/\lambda_{SP} < 2$ is satisfied by Sample#2.3, Sample#2.4, Sample#2.5, Sample#2.6, Sample#2.7, and Sample#2.8. In this context, Talbot revivals are observed at specific Talbot distances, the Talbot revivals at integral Talbot positions τ_m and fractional revivals at fractional Talbot positions τ'_m. These positions and simulated Talbot distances of these samples are given in Table 7. Integral Talbot position τ is smaller than calculated paraxial Talbot distances τ_{cal} for both paraxial and non-paraxial approximations. Table 8, showing that Talbot clarity increases, yields intensity maps atop the structure surface and at τ_m and τ'_m for Sample#2.3, Sample#2.4, Sample#2.5, Sample#2.6, Sample#2.7, and Sample#2.8.

Table 8. Normalized intensity distributions at Talbot distances τ_m and fractional Talbot distances τ'_m. The period of the ticks on *x*- and *y*-axes is 2 μm.

	Sample#2.	***Sample#2.***	***Sample#2.***	***Sample#2.***	***Sample#2.***	***Sample#2.***
Atop the surface	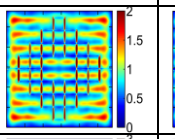	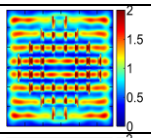	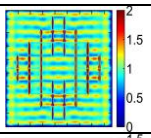	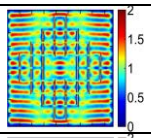	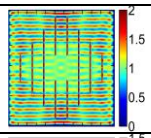	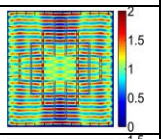
τ'_1	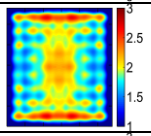	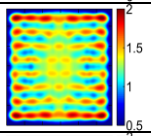	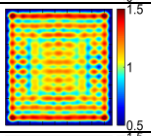	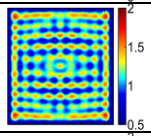	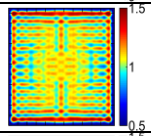	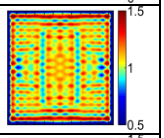
τ_1	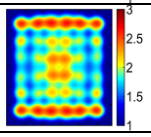	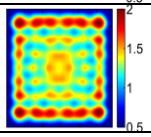	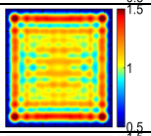	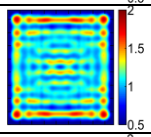	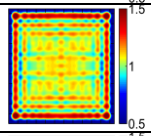	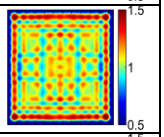
τ'_2			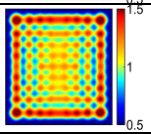	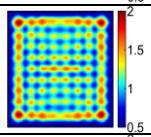	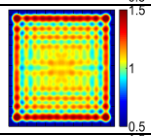	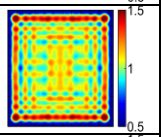
τ_2			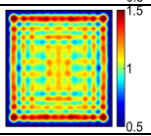	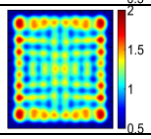	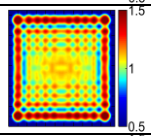	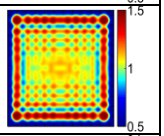
τ'_3					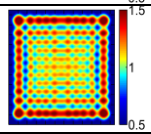	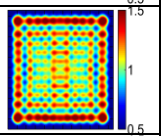
τ_3					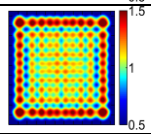	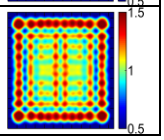

4. Conclusion

Consequently, a preliminary simulation study is handled for lensing by diffraction from Sierpinski carpet-based fractal lattice with alternative plasmonic material at communication wavelength. These finite-sized 2D designs have been investigated at 1st and 2nd iterations for various lattice length and lattice multiples of plasmon wavelength. Focusing performance parameters of this nanolattice system are evaluated in the air environment in detail via the 3D FDTD numerical simulation method. A conformal Talbot effect unlike ordinary Talbot effect yields an interesting focusing performance due to 2D finite-size, the periodicity, and fractal generation of the design. Additionally, diffraction-limited Talbot revivals are monitored in this conformal system since a diffraction-related fact, Talbot effect is can only be hold for a short distance due to the boundary effect. Thus, both plasmon Talbot effect and focusing behavior can be observed at the communication wavelength λ_0 = 1550 nm. According to simulation results, η_{foc} > 50% and η_{abs} > 18% have been introduced by all computational samples. It is observed both iteration increment for same geometrical parameters and geometrical parameter increment for same iteration provide longer focal length, larger focal depth than focal length, larger FWHM spot size, and smaller NA. NA values from 0.19 up to 0.97 and FWHM spot sizes from $0.81\lambda_0$ up to $5.6\lambda_0$ are proposed via this alternative plasmonic design. As a result, primary focal spots have low–cost and light capturing tolerance capturing tolerance, and narrower spot size through non-primary focal spots obtained on the sub-scales. Furthermore, this design with GZO material also ensures the conformal plasmon Talbot effect and focusing at 1550 nm-communication wavelength due to 2D finite-sized construction. Thus, a new nano-structured alternative plasmonic microlens design has been proposed as a planarized conformal transformation optics device.

Acknowledgement

The work described in this paper is supported by the Scientific Research Projects Coordination Center of Hatay Mustafa Kemal University (Project ID: 20.M.036).

Conflict of Interest

No conflict of interest was declared by the authors.

References

Aieta, F., Genevet, P., Kats, M. A., Yu, N., Blanchard, R., Gaburro, Z., Capasso, F., 2012. Aberration-Free Ultrathin Flat Lenses and Axicons at Telecom Wavelengths Based on Plasmonic Metasurfaces. Nano Letters, 12, 9, 4932-4936.

Arbabi, E., Arbabi, A., Kamali, S., Horie, Y., Faraon, A., 2016. Multiwavelength polarization-insensitive lenses based on dielectric metasurfaces with meta-molecules. Optica, 3, 628-633.

Arbabi, A., Horie, Y., Ball, A. J., Bagheri, M., Faraon, A., 2015. Subwavelength-thick lenses with high numerical apertures and large efficiency based on high-contrast transmitarrays. Nature Communications, 6, 7069.

Aouani, H., Rahmani, M., Torres, V., Hegnerova, K., Beruete, M., Homola, J., Hong, M., Navarro-Cía, M., Maier, S. A., 2013. Plasmonic Nanoantennas for Multispectral Surface-Enhanced Spectroscopies. The Journal of Physical Chemistry C, 117, 18620-18626.

Aslan, E., Aslan, E., Saracoglu, O. G., Turkmen, M., 2019. An effective triple-band enhanced-infrared-absorption detection by honeycomb-shaped metamaterial-plasmonic absorber. Sensors and Actuators A: Physical, 288, 149-155.

Aslan, E., Aslan, E., Turkmen, M., Saracoglu, O. G., 2017. Metamaterial plasmonic absorber for reducing the spectral shift between near- and far-field responses in surface-enhanced spectroscopy applications. Sensors and Actuators A: Physical, 267, 60-69.

Aslan, E., Aslan, E., Wang, R., Hong, M.K., Erramilli, S., Turkmen, M., Saracoglu, O.G., Dal Negro, L., 2016. Multispectral Cesaro-Type Fractal Plasmonic Nanoantennas. ACS Photonics, 3, 11, 2102-2111.

Aslan, E., Kaya, S., Aslan, E., Korkmaz, S., Saracoglu, O. G., Turkmen, M., 2017. Polarization insensitive plasmonic perfect absorber with coupled antisymmetric nanorod array. Sensors and Actuators B: Chemical, 243, 617-625.

Barnes, W. L., 2006. Surface plasmon–polariton length scales: a route to sub-wavelength optics. Journal of Optics A: Pure and Applied Optics, 8, S87–S93.

Berini, P., 2014. Surface plasmon photodetectors and their applications. Laser & Photonics Reviews, 8, 197–220.

Byrnes, S., Lenef, A., Aieta, F., Capasso, F., 2016. Designing large, high-efficiency, high-numerical-aperture, transmissive meta-lenses for visible light. Optics Express, 24, 5110-5124.

Dennis, M., Zheludev, N., Javier García de Abajo, F., 2007. The plasmon Talbot effect. Optics Express, 15, 9692-9700.

Gao, H., Hyun, J. K., Lee, M. H., Yang, J.-C., Lauhon, L. J., Odom, T. W., 2010. Broadband Plasmonic Microlenses Based on Patches of Nanoholes. Nano Letters, 10, 4111-4116.

Gao, X.-Z., Pan, Y., Zhao, M.-D., Zhang, G.-L., Zhang, Y., Tu, C., Li, Y., Wang, H.-T., 2018. Focusing behavior of the fractal vector optical fields designed by fractal lattice growth model. Optics Express, 26, 1597-1614.

Gottheim, S., Zhang, H., Govorov, A. O., Halas, N. J., 2015. Fractal Nanoparticle Plasmonics: The Cayley Tree. ACS Nano, 9, 3284−3292.

Hua, Y., Suh, J., Zhou, W., Huntington, M., Odom, T., 2012. Talbot effect beyond the paraxial limit at optical frequencies. Optics Express, 20, 14284-14291.

Khorasaninejad, M., Chen, W.T., Devlin, R.C., Oh, J., Zhu, A.Y., Capasso, F., 2016. Metalenses at visible wavelengths: Diffraction-limited focusing and subwavelength resolution imaging. Science, 352, 1190-1194.

Kim, Jo., Naik, G. V., Emani, N. K., Guler, U., Boltasseva, A., 2013. Plasmonic Resonances in Nanostructured Transparent Conducting Oxide Films. IEEE Journal of Selected Topics in Quantum Electronics, 19, 4601907.

Lalanne, P., Chavel, P., 2017. Metalenses at visible wavelengths: past, present, perspectives. Laser & Photonics Reviews, 11, 1600295.

Li, B., Piyawattanametha, W., Qiu, Z., 2019.Metalens-Based Miniaturized Optical Systems. Micromachines, 10, 310.

Li, L., Fu, Y., Wu, H., Zheng, L., Zhang, H., Lu, Z., Sun, Q., Yu, W., 2011. The Talbot effect of plasmonic nanolenses. Optics Express, 19, 19365-19373.

Li, W., Li, H., Gao, B., Yu, Y., 2017. Investigation on the plasmon Talbot effect of finite-sized periodic arrays of metallic nanoapertures. Scientific Reports, 7, 45573.

Liu, K., Li, N., Sadana, D. K., Sorger, V. J., 2016. Integrated Nanocavity Plasmon Light Sources for On-Chip Optical Interconnects. ACS Photonics, 3, 233-242.

MacDonald, K. F., Samson, Z. L., Stockman, M. I., Zheludev, N.´I., 2009. Ultrafast active plasmonics. Nature Photonics, 3, 55−58.

Mandelbrot, B.B., 1982. The Farctal Geometry of Nature, W. H. Freeman and Company.

Mehdi, A.-B., Luo, X.-P., Li, C.-B., Feng, S., Dong, M., Zhu, L.-Q., 2018a. The Observation of Plasmonic Talbot Effect at Non-Illumination Side of Groove Arrays. Plasmonics, 13, 2387–2394.

Mehdi, A.-B., Lou, X.-P., Dong, M.-L., Li, C.-B., Feng, S., Saviz, P., Zhu, L.-Q., 2018b. Geometrical condition for observing Talbot effect in plasmonics infinite metallic groove arrays. Chinese Physics B, 27, 124204.

Minovich, A. E., Miroshnichenko, A.E., Bykov, A.Y., Murzina, T.V., Neshev, D.N., Kivshar, Y.S., 2015. Functional and nonlinear optical metasurfaces. Laser & Photonics Reviews, 9, 195-213.

Naik, G. V., Shalaev, V. M., Boltasseva, A., 2013. Alternative Plasmonic Materials: Beyond Gold and Silver. Advanced Materials. 2013, 25, 3264-3294.

Rayleigh, L.,1881. XXV. On copying diffraction-gratings, and on some phenomena connected therewith, The London, Edinburgh, and Dublin Philosophical Magazine and Journal of Science, 11(67), 196-205.

Rosa, L., Sun, K., Juodkazis, S., 2011. Sierpin´ski fractal plasmonic nanoantennas. Physica Status Solidi RRL, 5−6, 175−177.

Talbot, H.F., 1836. LXXVI. Facts relating to optical science. No. IV, The London, Edinburgh, and Dublin Philosophical Magazine and Journal of Science, 9(56), 401-407.

Tanriover, I., Demir, H. V., 2019. Broad-band polarization-insensitive all-dielectric metalens enabled by intentional off-resonance waveguiding at mid-wave infrared. Applied Physics Letters, 114, 043105.

Vogt M. R., 2015. PhD. Thesis, Gottfried Wilhelm Leibniz Universität Hannover.
Volpe, G.; Volpe, G.; Quidant, R., 2011. Fractal Plasmonics: Subdiffraction Focusing and Broadband Spectral Response by a Sierpinski Nanocarpet. Optics Express, 19, 3612-3618.
Wang, E.-W., Li, L.-L., Yu, W.-X., Wang, T.-S., Gao, J.-S., Fu, Y.-Q., Liu, Y.-L., 2013. The Focusing Property of Immersed Plasmonic Nanolenses Under Radially Polarized Illumination. IEEE Photonics Journal, 4500207.
Wen, J., Zhang, Y., Xiao, M., M. 2013. The Talbot effect: recent advances in classical optics, nonlinear optics, and quantum optics. Advances in Optics and Photonics, 5, 83-130.
Xia, T., Cheng, S., Tao, S., 2019. A general n-fractal aperiodic zone plate. Journal of Modern Optics, 66 (11), 1179–1189.
Yang, Y., Dai, H. T., Sun, X. W., 2014. Fractal diabolo antenna for enhancing and confining the optical magnetic field. AIP Advances, 4, 017123.
Yu, N., Capasso, F., Flat optics with designer metasurfaces. Nature Materials, 13, 139–150.
Yu, Y., Chassaing, D., Scherer, T., Landenberger, B., Zappe, H., 2013. The Focusing and Talbot Effect of Periodic Arrays of Metallic Nanoapertures in High-Index Medium. Plasmonics 2013, 8, 723-732.
Zang, H.P., Zheng, C.L., Ji, Z.W., Fan, Q.P., Wei, L., Li, Y.J., Mu, K.J., Chen, S., Wang, C. K., Zhu, X.L., 2019. Characterization of focusing performance of spiral zone plates with fractal structure. Chinese Physics B, 28, (6) 064201.
Zhang, L., Mei, S., Huang, K., Qiu, C.W., 2016. Advances in Full Control of Electromagnetic Waves with Metasurfaces. Advanced Optical Materials, 4, 818-833.
Zhang, W., Zhao, C., Wang, J., Zhang, J., 2009. An experimental study of the plasmonic Talbot effect. Optics Express, 17, 19757-19762.